

## Highlights

### **Progressive augmentation of Reynolds stress tensor models for secondary flow prediction by computational fluid dynamics driven surrogate optimisation**

Mario Javier Rincón, Ali Amarloo, Martino Reclari, Xiang I. A. Yang, Mahdi Abkar

- Two models with different levels of complexity have been developed to augment the  $k - \omega$  SST turbulence model for the prediction of secondary flows.
- The progressive approach involves improving the linear eddy-viscosity model's capacity to predict secondary flows, without compromising its successful performance in canonical flows.
- The new explicit algebraic Reynolds stress correction models (EARSCMs) are able to predict secondary flows in contrast to common linear eddy-viscosity models.
- CFD-driven surrogate optimisation has proven to be a robust method to obtain enhanced models that do not compromise the solver's stability.
- The surrogate and Pareto-front solutions obtained are validated numerically and the best models obtained are verified against a series of canonical cases where their performance has been quantified.

# Progressive augmentation of Reynolds stress tensor models for secondary flow prediction by computational fluid dynamics driven surrogate optimisation

Mario Javier Rincón<sup>a,1,\*\*</sup>, Ali Amarloo<sup>a,\*\*</sup>, Martino Reclari<sup>b</sup>, Xiang I. A. Yang<sup>c</sup>, Mahdi Abkar<sup>a,\*</sup>

<sup>a</sup>Department of Mechanical and Production Engineering, Aarhus University, 8200 Aarhus N, Denmark

<sup>b</sup>Quality & Sustainability Department, Kamstrup A/S, 8660 Skanderborg, Denmark

<sup>c</sup>Department of Mechanical Engineering, Pennsylvania State University, State College, PA, 16802, USA

---

## Abstract

Generalisability and the consistency of the *a posteriori* results are the most critical points of view regarding data-driven turbulence models. This study presents a progressive improvement of turbulence models using simulation-driven surrogate optimisation based on Kriging. We aim for the augmentation of secondary-flow reconstruction capability in a linear eddy-viscosity model without violating its original performance on canonical cases e.g. channel flow. Explicit algebraic Reynolds stress correction models (EARSCMs) for  $k - \omega$  SST turbulence model are obtained to predict the secondary flow which the standard model fails to capture. The optimisation of the models is achieved by a multi-objective approach based on duct flow quantities, and numerical verification of the developed models is performed for various test cases. The results of testing new models on channel flow cases guarantee that new models preserve the performance of the original  $k - \omega$  SST model. Regarding the generalisability of the new models, results of unseen test cases demonstrate a significant improvement in the prediction of secondary flows and streamwise velocity. These results highlight the potential of the progressive approach to enhance the performance of data-driven turbulence models for fluid flow simulation while preserving the robustness and stability of the solver.

*Keywords:* Turbulence modelling, RANS, Progressive augmentation, Surrogate modelling, Kriging, Secondary flows

---

## 1. Introduction

Reynolds-averaged Navier-Stokes (RANS) equations are widely preferred over high-fidelity methods like direct numerical simulation (DNS) and large-eddy simulation (LES) for the industrial applications of computational fluid dynamics (CFD) due to their robustness and computational speed. In RANS, the physics of turbulence is modelled by a Reynolds stress tensor (RST) model; hence, the obtained results are dependent on the performance of these models. Despite the popularity of RANS simulations, the common empirical models have been found to have shortcomings [1], particularly in capturing secondary flows [2]. This limitation is accentuated in the most commonly used RANS turbulence models (e.g. two-equation models based on the Boussinesq assumption like  $k - \varepsilon$  and  $k - \omega$ ) due to their inability to predict complex turbulence anisotropy.

Although the development of reliable RANS turbulence models has remained stagnant for decades [3], the recent advances in data-driven techniques have motivated a new wave of studies seeking improvement for the performance of RANS turbulence models [4]. The majority of these studies have been trying to use the available high-fidelity data of the RST values to train a model to improve the results obtained from empirical models [5–10], to correct the RST prediction [11–15], or to modify the empirical models [16–18]. In a different approach, CFD-driven models [19, 20] have shown promising results in finding a reliable RANS turbulence model since they can guarantee consistency and robustness in *a posteriori* results. As opposed to other data-driven RANS models (i.e. by a *a priori*-training method

---

\*Corresponding author

\*\*M. J. Rincón and A. Amarloo contributed equally in this study.

Email address: abkar@mpe.au.dk (Mahdi Abkar)

[16]), CFD-driven models (i.e. by a model-consistent training method [16]) are optimised while performing RANS simulations to guarantee the improvement of the results obtained by new RANS models.

Design optimisation algorithms that aim to minimise or maximise one or more functions in a multi-dimensional parameter space are essential in engineering and scientific applications. Some of the commonly used optimisation algorithms include slope followers [21], simplex methods [22], multi-objective evolutionary algorithms [23], and particle swarm algorithms [24], among others. However, these algorithms require the evaluation of an objective function, which can be computationally expensive if CFD simulations are involved, especially in cases where a large number of test configurations are required.

To address this issue, development has been made towards the use of a relatively smaller set of simulations to create computationally efficient surrogate models, also known as response surfaces, that can then be fastly optimised. Response surfaces are mathematical models that approximate the behaviour of the objective function in the parameter space and can be used to predict the function values at untested configurations. This approach has been applied to various engineering applications, such as optimising complex internal-flow systems based on ultrasonic flow metering [25, 26], improving the efficiency of gas cyclones [27], optimising the aero-structural design of plane wings [28], and improving the performance of ground vehicles [29], among others.

However, the application of surrogate-based optimisation (SBO) methods to improve complex mathematical tools such as RANS turbulence modelling has not been widely explored. There are only a few studies that have investigated the use of optimisation algorithms and data-driven models for the improvement of the RANS turbulence models. Ref. [19] combined CFD-driven optimisation with gene expression programming to obtain a correction for the RST modelled by the  $k - \omega$  SST model. They showed that the CFD-driven model had an improved performance compared to the data-driven model trained on the same case. They concluded that CFD-driven models have a great potential for developing reliable improved RANS models even though their new model was limitedly optimised for wake mixing flow. The CFD-driven methodology was extended to a multi-objective optimisation for coupled turbulence closure models [30]. In another study, Ref. [20] used response surfaces to find the best linear combination of candidate functions to correct the RST values modelled by the  $k - \omega$  SST model for the cases with recirculation zone. They also showed that a CFD-driven approach yields models that perform better than the data-driven models trained on the same set of data. In Ref. [31], the authors resort to Kriging and obtained wall models for boundary layer flows subjected system rotation in an arbitrary direction. The model was shown to capture deviations in the mean flow from the equilibrium law of the wall. In Ref. [32], the authors employed an evolutionary neural network and arrived at numerical strategies for the pressure Poisson equation with density discontinuities.

Despite the existing research on data-driven models, the most important topic in data-driven RANS modelling is the generalisability of the new models for unseen cases [33]. Regarding this issue, Ref. [34] suggested using a multi-case CFD-driven approach to consider different turbulent phenomena during the optimisation process. They showed that a multi-case optimisation can help with the generalisability of the new model, however, their new models are still specific to either wall-free or wall-bounded flows; therefore, the generalisability problem requires further investigation.

The generalisability problem of data-driven models is not only limited to the unseen cases extrapolated out of the training cases range but they should be able to perform well on canonical cases like channel flow. Ref. [35] proposed the combination of a conventional progressive approach with data-driven approaches. In the progressive approach, the starting point is a baseline model that is already performing adequately for simple flows and adds more complexity step by step without violating the model's performance for the simple flow cases. In this study, we use the progressive approach to add the capability of secondary flow reconstruction to a linear eddy-viscosity model without violating its successful performance in a channel flow simulation.

Since the CFD-driven technique (i.e. model-consistent training method [16]) ensures the consistency of the *a posteriori* results and the progressive approach helps with the generalisability of the new models, in this study we combine the CFD-driven optimisation technique with the progressive approach to obtain an explicit algebraic Reynolds stress correction model (EARSCM) to the  $k - \omega$  SST [36] model for capturing secondary flows. Since all the standard linear eddy-viscosity models are inherently unable to capture secondary flows [2], we use the Pope's decomposition of RST [37] to add the non-linear term of the RST to the model, and we optimise the new models for the prediction of secondary flows induced by a duct flow with an aspect ratio (AR) of 1 (squared) at bulk Reynolds number of 3500 (depicted in Fig. 1). The new models' boundary-layer prediction is tested on the channel flow to ensure that they do not affect the performance of the original model. Considering the generalisability, the new models are verified on duct

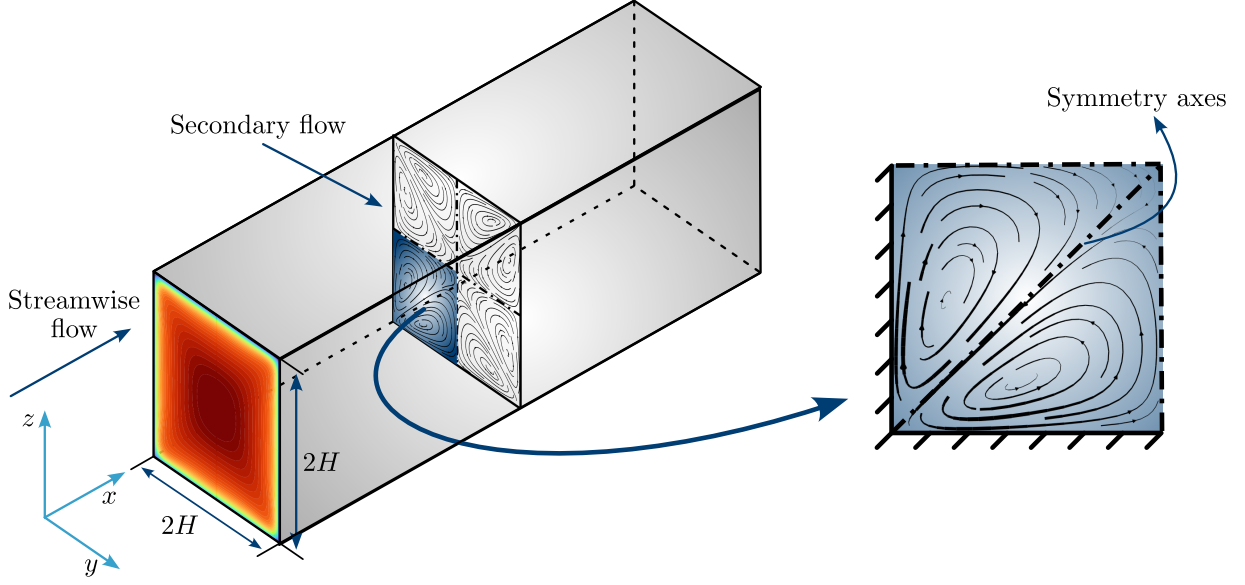


Figure 1: Flow characteristics of a duct flow with AR = 1 and height and width of  $2H$ . Note the formation of secondary motions and their symmetry.

flow cases with different Reynolds numbers and aspect ratios. Finally, to test the new models against an extremely disadvantageous case regarding accurate flow prediction by RANS models, we verify the new models in a case where the secondary flow is induced by roughness patches in a channel flow [38, 39] with a nominally infinite Reynolds number.

## 2. Methodology

This section presents the structure of the progressive correction model for RANS modelling and the optimisation technique for training the correction model. By using the Reynolds decomposition of velocity and pressure, the Navier-Stokes equation for an incompressible steady flow can be written as [40]

$$u_i = \langle u_i \rangle + u'_i, \quad p = \langle p \rangle + p', \quad (1)$$

$$\partial_i \langle u_i \rangle = 0, \quad \partial_j \langle u_i \rangle \langle u_j \rangle = -\frac{1}{\rho} \partial_i \langle P \rangle + \partial_j (v \partial_j \langle u_i \rangle - A_{ij}), \quad (2)$$

where  $i, j = 1, 2, 3$  are indicating the streamwise ( $x$ ), spanwise ( $y$ ), and vertical ( $z$ ) directions, respectively.  $u_i$  and  $p$  are velocity and pressure decomposed to a temporal mean term, indicated by  $\langle \cdot \rangle$ , and fluctuations, indicated by  $'$ .  $v$  is the kinematic viscosity, and  $\rho$  is the fluid density.  $A_{ij} = \langle u'_i u'_j \rangle - \frac{1}{3} \langle u'_k u'_k \rangle \delta_{ij}$  is the anisotropic part of RST, and pressure is modified with the isotropic part of the RST as  $\langle P \rangle = \langle p \rangle + \frac{1}{3} \rho \langle u'_i u'_i \rangle$ .

In this study, the  $k - \omega$  SST [36] model is used as a baseline model to be progressively corrected to predict secondary flows. In the standard  $k - \omega$  SST model,  $A_{ij}$  is modelled as

$$A_{ij}^{BL} = -2\nu_t S_{ij}, \quad (3)$$

where  $S_{ij} = \frac{1}{2}(\partial_i \langle u_j \rangle + \partial_j \langle u_i \rangle)$  is the strain rate tensor,  $\nu_t$  is the turbulent viscosity which is calculated by values of turbulent kinetic energy (TKE) (i.e.  $k$ ), and the specific dissipation rate (i.e.  $\omega$ ), which are modelled by the original two-equation model [41].

### 2.1. Progressive EARSCM

We extend the structure of the linear eddy-viscosity model (Eq.3) by following Pope's decomposition [37] of the RST, by considering the two first terms of the decomposition,

$$A_{ij} = 2k\alpha^{(1)}\frac{S_{ij}}{\omega} + 2k\alpha^{(2)}\frac{S_{ik}\Omega_{kj} - \Omega_{ik}S_{kj}}{\omega^2}, \quad (4)$$

where  $\Omega_{ij} = \frac{1}{2}(\partial_i\langle u_j \rangle - \partial_j\langle u_i \rangle)$  is the rotation rate tensor, and  $\alpha^{(n)}$  are unknown functions of 5 invariants defined as,

$$I_1 = \frac{\text{tr}(S_{ik}S_{kj})}{\omega^2}, I_2 = \frac{\text{tr}(\Omega_{ik}\Omega_{kj})}{\omega^2}, I_3 = \frac{\text{tr}(S_{ik}S_{km}S_{mj})}{\omega^3}, I_4 = \frac{\text{tr}(\Omega_{ik}\Omega_{km}S_{mj})}{\omega^3}, I_5 = \frac{\text{tr}(\Omega_{ik}\Omega_{km}S_{ml}S_{lj})}{\omega^4}. \quad (5)$$

A comparison between Eq. 3 and Eq. 4 shows that the  $k-\omega$  SST model is already providing the first term in Pope's decomposition of the RST; therefore following the progressive approach, only the second term is trained in this study. Hence, the new RST model can be written as

$$A_{ij} = -2\nu_t \left( S_{ij} - \alpha^{(2)} \frac{S_{ik}\Omega_{kj} - \Omega_{ik}S_{kj}}{\omega} \right) \quad (6)$$

where  $\nu_t$  and  $\omega$  are modelled by the standard  $k-\omega$  SST model, and the unknown function of  $\alpha^{(2)}$  is determined by the CFD-driven optimisation technique. It should be mentioned that the linear part of the new model is treated implicitly as turbulent viscosity, and the non-linear part of the RST is added explicitly to the RANS equations.

Inspired by a sparse regression of candidate functions (SpaRTA) [14] used for  $\alpha^{(n)}$ , we use a set of candidate functions to describe  $\alpha^{(2)}$  as

$$\alpha^{(2)} = \theta_0 + \sum_{i=1}^{20} \theta_i \mathcal{D}_i, \quad (7)$$

$$\begin{aligned} \mathcal{D} = \{ & I_1, I_2, I_3, I_4, I_5, I_1^2, I_2^2, I_3^2, I_4^2, I_5^2, \\ & I_1 I_2, I_1 I_3, I_1 I_4, I_1 I_5, I_2 I_3, I_2 I_4, \\ & I_2 I_5, I_3 I_4, I_3 I_5, I_4 I_5 \}, \end{aligned} \quad (8)$$

where  $\theta_i$  are constant coefficients to be determined by the CFD-driven optimisation process. To achieve a more efficient sparse optimisation, the normalised candidate functions are normalised and defined as

$$\mathcal{B}_i = \frac{\mathcal{D}_i - \mu_i}{\sigma_i}, \quad (9)$$

where  $\mu_i$ ,  $\sigma_i$  are the mean and the standard deviation of each candidate function  $\mathcal{D}_i$ , respectively. These statistics are calculated based on high-fidelity data from the optimisation case. Therefore, Eq. 7 is rewritten as,

$$\alpha^{(2)} = C_0 + \sum_{i=1}^{20} C_i \mathcal{B}_i, \quad (10)$$

where an optimisation technique determines the coefficients  $C_i$  based on the performance of the correction model for the reconstruction of the high-fidelity velocity field of a optimisation case.

Since considering 21 optimisation variables is impractical, making the model unnecessarily complex and exposed to solution instabilities, two approaches are chosen:

1. Selecting only the first  $m$  leading candidate functions.
2. Reducing the dimensionality of the problem using a statistical technique.

Both of these approaches are compared, and for the purpose of dimensionality reduction, principal component analysis (PCA) is applied on the  $\mathcal{B}_i$  functions to obtain the first  $m$  principal components as,

$$\varphi_j = \sum_{i=1}^{20} a_i^{(j)} \mathcal{B}_i, \quad (11)$$

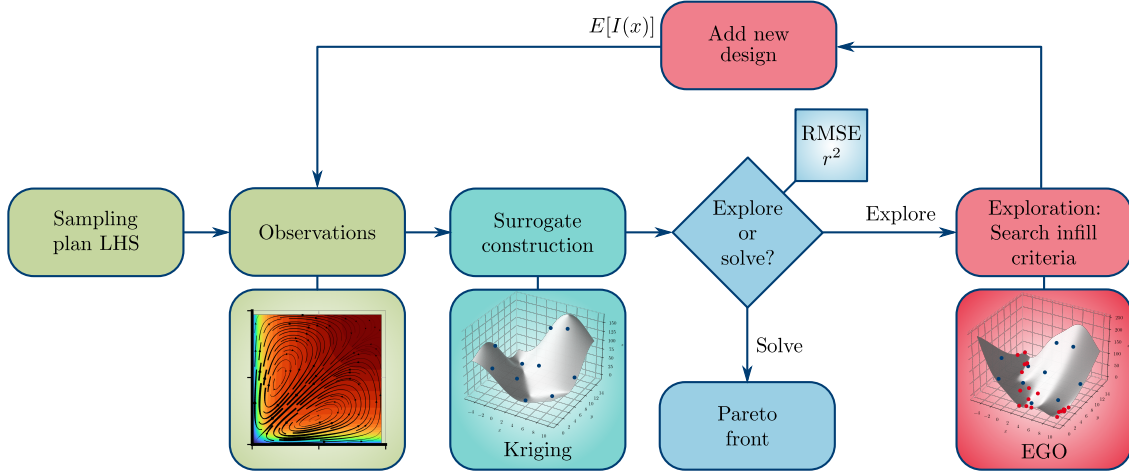


Figure 2: Design optimisation strategy employed involving an initial sampling plan based on Latin hypercube sampling (LHS) which is solved by CFD. Subsequently, an initial surrogate is constructed using Kriging. Since it is likely that the initial sampling may not evaluate the surrogate in extrema, Bayesian strategies based on efficient global optimisation (EGO) and the evaluation of the expected improvement ( $E[I(x)]$ ) function are then applied to further explore the surrogate and improve its quality. Finally, once the quality requirements have been met, a genetic algorithm is employed to search for non-dominated optima on the surrogate model.

where the coefficients  $a_i^{(j)}$  are obtained by performing PCA on the high-fidelity data from the optimisation case. By considering this transformation equation, Eq. 10 is rewritten as,

$$\alpha^{(2)} = C_0 + \sum_{i=1}^m C_i \varphi_i. \quad (12)$$

Based on the high-fidelity data of the optimisation case, in Sec. 3.1 it is shown that the first two principal components are enough to represent the variability of the dataset (i.e.  $m = 2$ ). Therefore, two different structures for  $\alpha^{(2)}$  are considered:

$$\alpha_I^{(2)} = C_0 + C_1 \mathcal{B}_1 + C_2 \mathcal{B}_2, \quad (13a)$$

$$\alpha_{II}^{(2)} = C_0 + C_1 \varphi_1 + C_2 \varphi_2, \quad (13b)$$

which are described as *model I* and *model II*, respectively. Where a unique set of three coefficients  $C_0$ ,  $C_1$ , and  $C_2$  are determined by a multi-objective optimisation technique for each of the models.

## 2.2. Optimisation methods

To approach the optimisation problem, a surrogate based on Kriging and Gaussian processes (GPs) is built. The surrogate is based on the design and analysis of computer experiments (DACE) [42], using observations obtained from a sequence of CFD solutions and post-processing of results. To assess the model's performance, two main objective functions are established that involve streamwise velocity and streamwise vorticity, defining a multi-objective optimisation problem. An effective sampling plan is also outlined, and an infill criterion constrained by quality metrics is specified. Finally, the methodology is implemented using the general-purpose software OpenFOAM [43]. A flow diagram of the complete optimisation methodology is depicted in Fig. 2.

### 2.2.1. Objective functions

The principal issue that is assessed in this study is the complete lack of prediction of secondary flows in RANS turbulence models based on the Boussinesq assumption. In the chosen optimisation case, the addition of these secondary flow motions is strong enough to also incur changes in the streamwise direction of the flow, hence, the correct prediction of the streamwise flow direction is also a key parameter to assess.

To holistically evaluate the flow prediction, the normalised error of both the streamwise velocity and vorticity with respect to high-fidelity data, are evaluated and taken as objectives to be minimised. To yield a fair and accurate single value representing these quantities, the volumetric average of each field is computed as the objective functions, following

$$j_1 = \frac{\int_V (\langle u_1 \rangle_{\text{EARSCM}} - \langle u_1 \rangle_{\text{HF}}) dV}{\int_V (|\langle u_1 \rangle_{k-\omega} - \langle u_1 \rangle_{\text{HF}}|) dV}, \quad (14a)$$

$$j_2 = \frac{\int_V (\langle \omega_1 \rangle_{\text{EARSCM}} - \langle \omega_1 \rangle_{\text{HF}}) dV}{\int_V (|\langle \omega_1 \rangle_{k-\omega} - \langle \omega_1 \rangle_{\text{HF}}|) dV}, \quad (14b)$$

where  $|\cdot|$  is the absolute value operation,  $\langle \omega_i \rangle = \varepsilon_{ilk} \partial_l \langle u_k \rangle$  is the vorticity of the mean flow, where  $\varepsilon_{ilk}$  is the alternating unit tensor, HF stands for high fidelity, and  $k-\omega$  refers to the solution of the standard  $k-\omega$  SST model. The definition of these functions yields a value of 1 when their output matches the prediction of  $k-\omega$  SST and 0 when the predictions match the high-fidelity data. Subsequently, to evaluate the overall results of the method, a global fitness function is defined as

$$J = \frac{1}{2} (j_1 + j_2). \quad (15)$$

### 2.2.2. Sampling plan

Two main algorithms are used in order to sample observations and data in this study: Monte Carlo and Latin hypercube. Monte Carlo sampling is used when extracting a test subset to compute the surrogate quality. Since the chosen sampling plan for the initial observations is oriented to be *space-filling*, Latin Hypercube Sampling (LHS) [44] with optimised design by the enhanced stochastic evolutionary (ESE) algorithm [45, 46] is used to obtain an initial sample of the surrogate with a minimum number of observations, and simultaneously, representing the real variability of the parameters. The initial sample by LHS with ESE follows  $n_0 = 30\mathcal{K}$ , where  $n_0$  is the initial number of observations, and  $\mathcal{K}$  is the number of design variables.

### 2.2.3. Surrogate construction

In the context of a sparse optimisation problem, surrogates are commonly used to approximate a function  $y = f(x)$  based on known observations. In this study, the Kriging method is chosen for generating the surrogate based on CFD-driven observations. Kriging is one of the most common surrogate construction methods due to its well-known implementation, ability to compute uncertainties and speed. Furthermore, it has been proven useful in physical, uncertainty quantification, and engineering applications [26, 47]. Kriging interpolates the observations as a linear combination of a deterministic term and a stochastic process, which is represented by

$$\hat{f}(x) = \sum_{i=1}^k \beta_i f_i(x) + Z(x), \quad (16)$$

where  $\hat{f}(x)$  is the surrogate prediction,  $\beta$  is a linear deterministic model,  $f(x)$  is the known function, and  $Z(x)$  is the realisation of a stochastic process with zero mean and spatial covariance function given by

$$\text{cov} [Z(x^{(i)}), Z(x^{(j)})] = \sigma^2 R(x^{(i)}, x^{(j)}). \quad (17)$$

Here, the spatial correlation function  $R$  determines how smooth the Kriging model is, how easily the response surface can be differentiated, and how much influence the nearby sampled points have on the model. In this study, the spatial correlation is defined following the squared exponential (Gaussian) function as

$$\prod_{i=1}^{nx} \exp \left[ -\theta_l (x_l^{(i)} - x_l^{(j)})^2 \right], \quad \forall \theta_l \in \mathbb{R}^+, \quad (18)$$

where the correlation matrix  $\theta_l$  is used to define the variance of a Gaussian process at each point, with higher values indicating a stronger correlation between points. By maximising the maximum likelihood estimation, optimal values for hyper-parameters as the matrix  $\theta_l$ , mean, and standard deviation can be found [48].

#### 2.2.4. Quality metrics

The quality of the surrogate refers to how accurately it approximates the true function being modelled. In order to evaluate this quality, a number of random test observations  $n_t = n_0$   $x \rightarrow y$ , are taken. where  $n_t$  is a function of the number of initial observations. Once the test observations have been generated, they are used to compare the surrogate's predictions to the true values of the function being modelled. The root-mean-squared error (RMSE) and Pearson's correlation coefficient squared ( $r^2$ ), defined as

$$\text{RMSE} = \sqrt{\frac{\sum_{i=1}^{n_t} (y^{(i)} - \hat{y}^{(i)})^2}{n_t}}, \quad (19a)$$

$$r^2 = \left( \frac{\text{cov}(y, \hat{y})}{\sqrt{\text{var}(y)\text{var}(\hat{y})}} \right)^2, \quad (19b)$$

are two common metrics used to evaluate the quality of surrogates. While the RMSE measures the difference between the surrogate's predictions and the true values,  $r^2$  measures the strength of its linear relationship. A high RMSE and a low  $r^2$  indicate that the surrogate is performing poorly and needs to be refined, while a low RMSE and a high  $r^2$  indicate that the surrogate is performing accurately and can be used with confidence. Hence, these values serve as reference points to determine whether the surrogate model is accurate enough to be used in the optimisation process.

In this study, thresholds of 0.2 for RMSE and 0.8 for  $r^2$  are established as indicators of good surrogate quality, based on previous studies [49, 50].

#### 2.2.5. Infill space exploration

Efficient global optimisation (EGO) based on Bayesian optimisation strategies is used to improve the accuracy of surrogate models and decrease overall uncertainty [51, 52]. This is achieved by exploring the surrogate beyond the initial sampling. EGO is a well-known algorithm that employs both local and global searches to find the optimal solution by means of the expected improvement ( $E[I(x)]$ ) function as a key metric to direct its search. The function calculates the potential improvement that can be obtained by evaluating a new observation point based on the current best solution and the overall uncertainty of the surrogate model [53]. The expected improvement function is defined as

$$E[I(x)] = (f_{\min} - \mu(x)) \Phi\left(\frac{f_{\min} - \mu(x)}{\sigma(x)}\right) + \sigma(x)\phi\left(\frac{f_{\min} - \mu(x)}{\sigma(x)}\right), \quad (20)$$

where  $f_{\min} = \min Y$ , and  $\Phi(\cdot)$  and  $\phi(\cdot)$  are respectively the cumulative and probability density functions of  $\mathcal{N}(0, 1)$ , following the distribution  $\mathcal{N}(\mu(x), \sigma^2(x))$ . Using EGO to explore the surrogate beyond the initial sampling aids in decreasing the overall uncertainty and improving the precision of the surrogate model, especially in the unexplored and extreme regions of the design space. Consequently, the algorithm can effectively balance local and global searches and locate the optimal solution more proficiently. Hence, the following sampling point is determined by

$$x_{n+1} = \arg \max_x (E[I(x)]). \quad (21)$$

In order to fully explore the design space, new data is collected for each objective function separately. This involves taking one sample of  $n_{\text{EGO}} = n_0$   $x \rightarrow y$  for each objective, resulting in a total of 60 new sampled points ( $n_0$  for each of the objectives). However, since the design space explored is large and the use of Bayesian optimisation might sample observations in very close proximity, the gradients between points may be high, yielding possible noise. Therefore, the methodology evaluates this noise and applies L1 regularisation to obtain a smooth response surface.

#### 2.2.6. Multi-objective solution

The Kriging method offers a significant benefit since it allows the application of algorithms that can thoroughly explore the objective space. Consequently, the objective of this study is to find the optimal solution for the surrogate model. To achieve this, the multi-objective evolutionary algorithm (MOEA) NSGA-II has been chosen. This algorithm is known for its versatility, fast and efficient convergence, and ability to handle non-penalty constraints. It also has a wide-range search for solutions, which implies that it can explore the objective space more thoroughly and is less likely



to get grounded in local optima [54]. By using the MOEA NSGA-II algorithm, the improved solutions are ensured to be non-dominated, meaning that they are not worse than any other feasible solution in all objective functions. This also ensures that the solutions avoid local minima and are highly likely to discover the global optimum for the sampled response surface. This makes the algorithm able to search a large portion of the objective space and find the best possible solution for the surrogate model while avoiding suboptimal solutions.

### 2.3. High-fidelity data

Since the main purpose of this study is to obtain an EARSCM for capturing the secondary flow, the DNS data of a canonical case with this flow characteristic is chosen. A duct flow case of AR= 1 and bulk Reynolds number of  $Re_b = 3500$  is used for the training process (depicted in Fig. 1). The DNS data is obtained from Ref. [55] curated by Ref. [56]. Following the progressive approach, the trained EARSCMs are tested on two cases of channel flow with friction Reynolds number of  $Re_\tau = 395$  and  $Re_\tau = 5200$  for which data is obtained from Refs. [57] and [58], respectively. Considering the generalisability of the new models, we likewise test them on three unseen cases containing secondary flows, including a duct secondary flow case with AR= 1 and higher bulk Reynolds number of  $Re_b = 5700$  [59], a duct secondary flow case with AR= 3, and a lower bulk Reynolds number of  $Re_b = 2600$  [59], and a roughness-induced secondary flow with nominally infinite Reynolds number (more information about the geometry and properties of this case is available at Refs. [15, 39]).

## 3. Results and discussion

In this section, the results are presented in two subsections. In the first one, the results of the optimisation process and training of the two best EARSCMs are presented, whereas, in the second, the performance of the trained models is evaluated on the test cases with different geometries, Reynolds numbers, and boundary conditions. Associated contours and velocity profiles accompany all results which are similarly described and discussed, followed by their corresponding figures.

### 3.1. Surrogate-based optimisation

#### 3.1.1. Optimisation case: $k - \omega$ SST performance

It is essential to qualitatively indicate the original performance of  $k - \omega$  SST against high-fidelity data prior to any modifications. For both fidelity levels, the results for the square duct case show the progressive deceleration of the streamwise flow as it approaches the walls of the duct, exhibiting higher gradients in the near-wall regions as a consequence of the boundary layer and the fully-developed turbulent flow. Whereas this behaviour can be predicted by  $k - \omega$  SST, the presence of a secondary flow captured by DNS is completely neglected by the RANS model (Fig. 3), as expected [2]. Two antisymmetric rotational regions are generated diagonally at the duct's vertex, preserving their symmetry at the 4 quadrants of the duct. This secondary flow is strong enough to drive the streamwise flow towards the duct vertices, skewing the streamwise velocity field in the domain through an impinging-like flow behaviour. Since  $k - \omega$  SST does not predict these rotational motions, the streamwise velocity distribution is not skewed and the spanwise and vertical components of the velocity are zero.

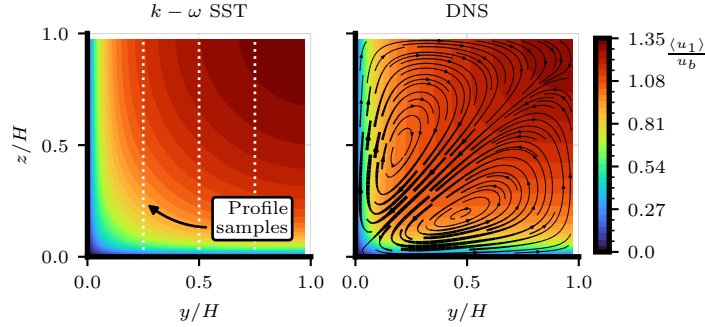


Figure 3: Contours of streamwise velocity and secondary flow streamlines for duct flow optimisation case at  $AR=1$  and  $Re_b = 3500$  for RANS  $k - \omega$  SST (left) and DNS (right) data. DNS data obtained from Ref. [55]. The dotted white lines denote the location of the velocity profiles evaluated throughout this study to perform a quantitative comparison. It should be noted the varying thickness of the secondary flow streamlines denotes their magnitude.

Figure 4 compares the barycentric plots representing the shape of RSTs for the optimisation case. The location of each point is calculated based on the eigenvalues of the normalised anisotropic part of the RST (more information about barycentric plots available at Refs. [60, 61]). While  $k - \omega$  SST yields all results within the plain-strain limit as expected from a linear eddy-viscosity RANS model, DNS shows a more complex stress anisotropy distribution as a combination of states toward one-component turbulence fluctuations  $\hat{x}_{1c}$  (also known as rod-like or cigar-like turbulence) and an offset from the plain-strain limit with a tendency towards isotropic (or spherical) turbulence  $\hat{x}_{3c}$ .

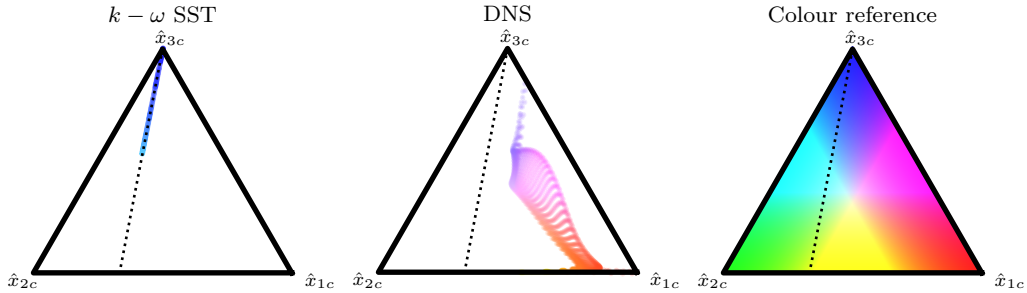


Figure 4: Reynolds stress anisotropy for  $k - \omega$  SST (left) and DNS (centre) for training duct flow case with  $AR=1$  at  $Re_b = 3500$ . DNS data obtained from Ref. [55]. The plain-strain limit is represented by the dotted line, and the colour representation (right) follows the work by [61].

### 3.1.2. Optimisation case: EARSCMs

Since  $k - \omega$  SST is not able to predict the secondary flow of the optimisation case, CFD-driven optimisation is applied following the models described in Eqs. 13a and 13b focusing on predicting secondary flows and correct streamwise velocity.

Regarding model II, PCA is applied to the set of candidate functions (listed in Eq. 8) using the high-fidelity data of the optimisation case. Figure 5 presents the PCA results and shows that only the first 2 principal components ( $\varphi_1$  and  $\varphi_2$ ) yield an explained variance ratio of 0.97 (Fig. 5a), where  $\varphi_1$  is the main principal component explaining the variability. Figure 5b presents the coefficients corresponding to the two first principal components used for model II.

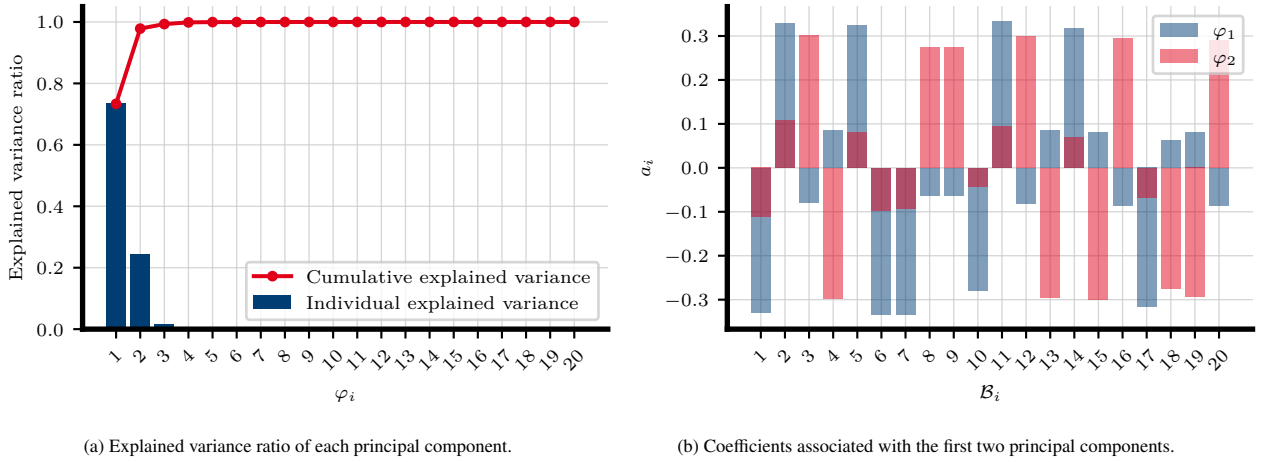


Figure 5: PCA results of the candidate functions calculated by DNS data of the optimisation case.

As mentioned in Sec. 2, the two first principal components for model *II* are chosen. To compare model *I* in an analogous manner, the two first leading candidate functions are likewise chosen. The coefficients of these two models are determined by a surrogate optimisation technique. A surrogate model is generated using the RANS simulations results to find the optimal values of the optimisation variables. Regarding the optimisation process and since cases with high values of the objective functions are not of interest, the MOEA optimisation is performed by imposing the constraint  $j_2 \leq 0.4$ , therefore, the analysed non-dominated solutions only take place in the regions of highest interest and potential global minimisation.

Regarding both models' results, an optimal design space of  $[-2, -1, -1] \leq C_i \leq [0, 1, 1]$  is chosen after various progressive surrogate iterations. The iterations re-define the design space limits by analysing the non-dominated values of the coefficients after optimisation. If these values are reaching the imposed limits, the objective space is reset, and the design space is adapted.

*Model I.* Contour plots in Fig. 6b illustrate how the optimisation variables affect the objective functions. On the one hand, the surrogate visualisation for  $j_1$  (Fig. 6a) shows a quasi-linear tendency for all variables. The global minimum for  $j_1$  is shown towards negative values for all  $C_i$  without clear visualisation of extrema. On the other hand, there is a clear global minimum seen for  $j_2$  values, shown by a non-linear surrogate for  $C_0$  and  $C_1$ , where quasi-linear behaviour is predicted by the relationship between  $C_1$  and  $C_2$  (Fig. 6b). It is important to highlight that, although the lowermost values for the coefficients predict an improvement for  $j_1$ , the tendency is not completely followed by  $j_2$  prediction. This incurs that a more accurate prediction of the streamwise flow does not necessarily correlate with the secondary flow prediction in this case.

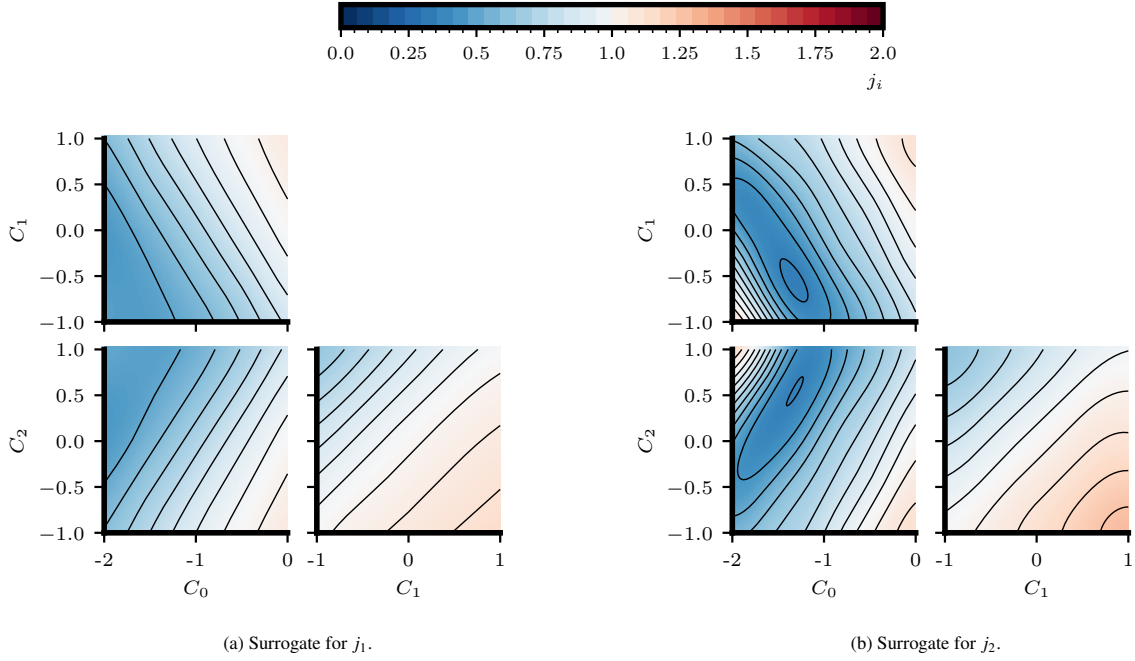


Figure 6: Surrogate contour visualisation. It should be noted that each pair of variables is shown by holding the other variable at zero.

Regarding the surrogate quality (Fig. 7a), and Pareto front prediction and numerical validation (Fig. 7b), the surrogate predicts the test set with great accuracy for the whole design space tested, which is likewise reflected by a highly accurate Pareto front prediction, where all numerical tests simulated are able to predict the objective space within  $1\sigma$  uncertainty bounds for both objective functions.

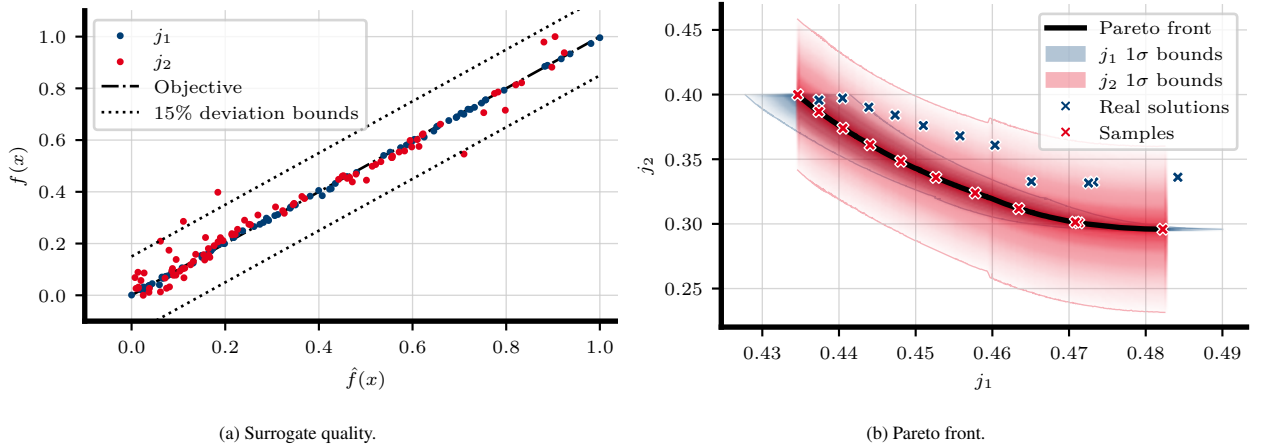


Figure 7: Surrogate quality against test set (Fig. 7a), and Pareto-front validation with  $1\sigma$  uncertainty bounds (Fig. 7b).

**Model II.** In contrast with model I, the surrogate visualisation for both objective functions (Fig. 8) in model II shows a non-linear prediction for all variables. This behaviour is somewhat expected due to the added complexity of the model with the PCA. The global minimum for  $j_1$  does not have a straightforward location. Instead, there are diverse regions where the global extrema can be found. Specifically, negative values of  $C_0$ , values of  $-0.5 \leq C_1 \leq 0.5$ , and  $0 \leq C_2 \leq 1$  predict generally lower values of  $j_1$  (Fig. 8a). Regarding  $j_2$ , there is a similar predicted behaviour compared to  $j_1$ : non-linear behaviour is shown  $C_i$ , and similar values of the coefficients tend to predict the location of

the minima (Fig. 8b). Similarly to model I, although the objective spaces for both functions follow similar tendencies, there are visible differences in the predicted locations of the minima, reflecting once more that a more accurate prediction of the streamwise flow does not necessarily correlate with the secondary flow prediction.

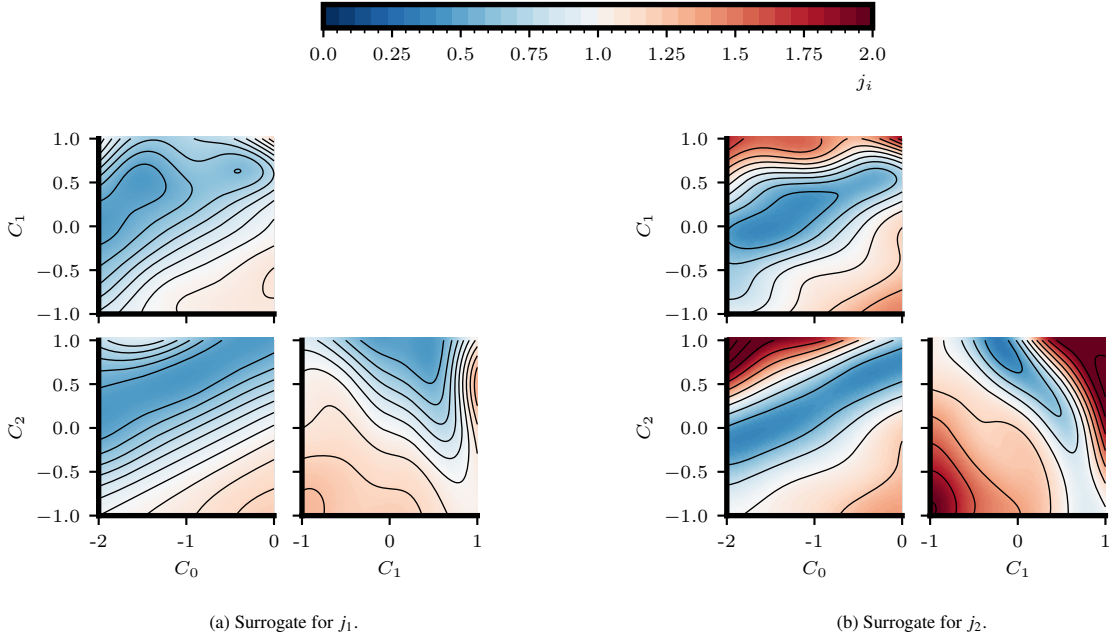


Figure 8: Surrogate contour visualisation. It should be noted that each pair of variables is shown by holding the other variable at zero.

Regarding the surrogate quality (Fig. 9a), and Pareto front prediction and numerical validation (8b), the surrogate predicts the test set with high accuracy for the whole design space tested, however, some outliers can be seen in the mid-range values of the objectives. These lower-confidence regions are not reflected in the non-dominated solutions nor in their numerical validation. Since the expected improvement function prioritises good confidence in the near-extrema region and the complexity of the model is higher, a certain level of uncertainty is expected in far-away regions of the global minimum. Nevertheless, the surrogate shows the same level of confidence at the Pareto front as model I (within  $1\sigma$ ).

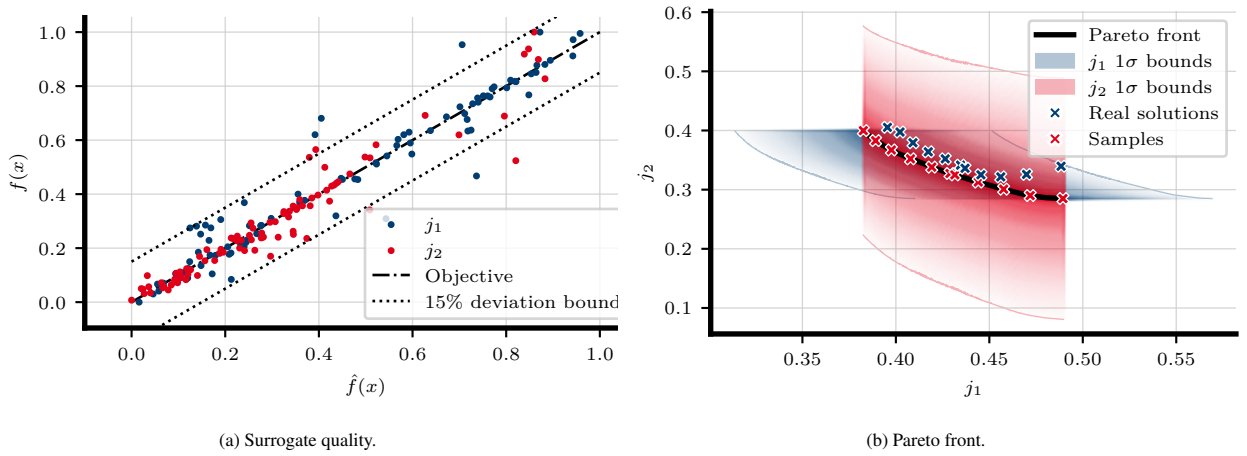


Figure 9: Surrogate quality against test set (Fig. 9a), and Pareto front validation with  $1\sigma$  uncertainty bounds (Fig. 9b).

### 3.2. Comparison of models

The final results for each model are shown in Table 1, where the best cases per model are shown, followed by their  $C_i$  values and surrogate quality parameters. Both models significantly improved the standard  $k - \omega$  SST by 61.3% and 62.7% for model **I** and **II** respectively. Differences in performance for the objective values alone are almost negligible, where model **II** is slightly showing better performance with a net  $J$  gain of 1.4%. Quality results of RMSE and  $r^2$  are reflected as previously seen in Fig. 7a, and 9a, where model **II** displays the best overall performance.

Table 1: Objective function results, coefficients, and quality for best models and surrogates of each approach

Model	$J$	$j_1$	$j_2$	$C_0$	$C_1$	$C_2$	RMSE <sub>1</sub>	RMSE <sub>2</sub>	$r_1^2$	$r_2^2$
<b>I</b>	0.387	0.455	0.319	-1.65	0.62	1	0.004	0.048	0.999	0.966
<b>II</b>	0.373	0.426	0.32	-0.17	-0.18	0.98	0.103	0.175	0.865	0.808

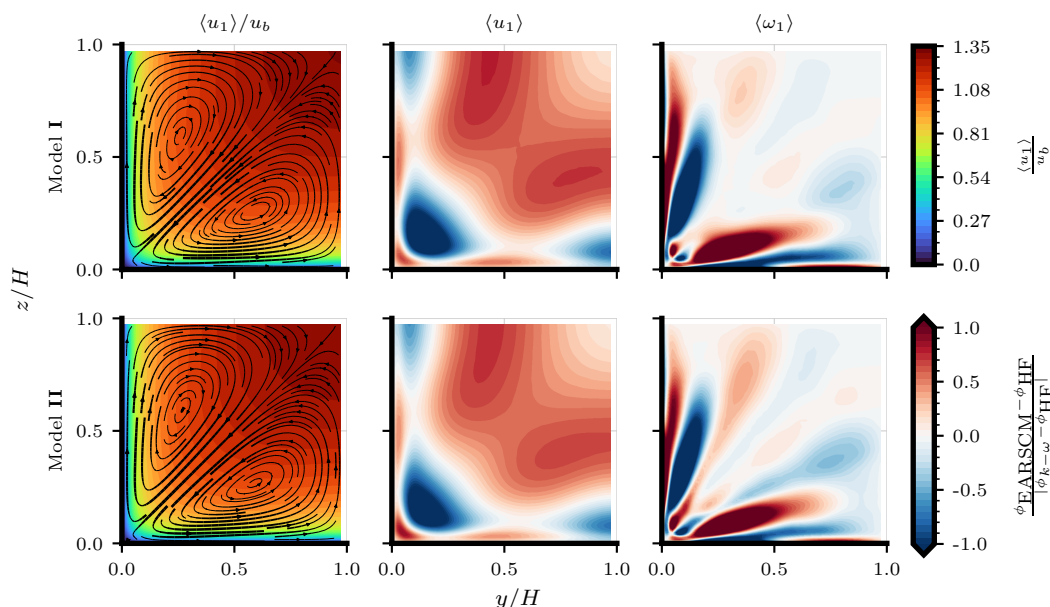


Figure 10: Qualitative streamwise and secondary flow prediction of the best cases for each of the models. Left: streamwise flow contours with stream function lines depicting secondary flow prediction and direction. Centre: streamwise flow error compared to DNS data. Right: streamwise vorticity error compared to DNS data. It should be noted that the stream function line thickness denotes the secondary flow intensity. In the colourbar,  $\phi$  indicates either  $\langle u_1 \rangle$  or  $\langle \omega_1 \rangle$ .

Regarding qualitative results for the optimisation case, both models are able to accurately capture the direction and symmetry of the secondary motions while improving the streamwise flow prediction. However, the secondary flow's magnitude generally is overpredicted, generally in the near-wall regions (Fig. 10). As a consequence of the prediction of a correct secondary flow direction, the streamwise flow prediction likewise improves. Regions of slight overprediction of  $\langle u_1 \rangle$  are seen in the near-wall regions as well as the middle section of the computational volume, whereas regions of  $\langle u_1 \rangle$  underprediction are seen in the bulk flow close to the channel vertex. Regarding the prediction of  $\langle \omega_1 \rangle$ , anti-symmetric predictions are seen with respect to the diagonal symmetry line with a general over and underprediction in the near-wall region.

As expected from the objective function results, qualitative differences between models (Fig. 11) are not clearly seen. For the streamwise velocity prediction, no significant differences can be seen in the contours of the error function, whereas for the vorticity prediction, slight variations in the error can be seen between models without a

significant impact on the overall performance of the models. Overall, both models are able to predict the secondary flow with high accuracy.

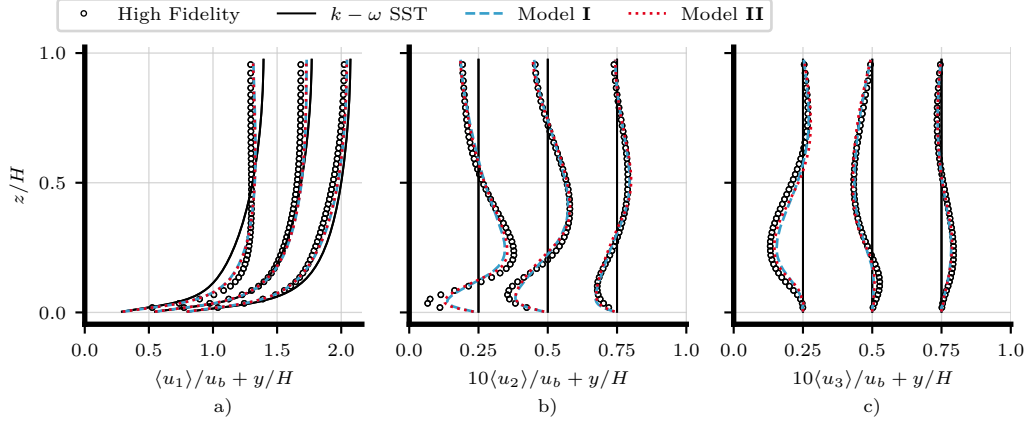


Figure 11: Profiles of velocity components for duct flow case with  $AR = 1$  and  $Re_b = 3500$ . High-fidelity data obtained from Ref. [55].

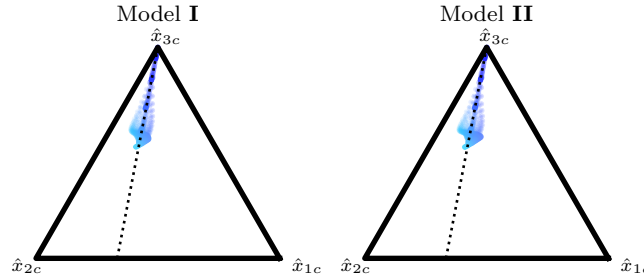


Figure 12: Barycentric map showing the physical reliability and turbulence anisotropy of the developed models following the colour representation by [61].

Concerning the quantitative analysis of the velocity profiles at  $y/H \in [0.25, 0.5, 0.75]$ , an overall and significant improvement in the prediction of both models against standard  $k - \omega$  SST, can be seen. Although the prediction of both models displays minor differences between each other, they both predict with high accuracy the DNS data. Some light discrepancy can be seen in the magnitudes at near-wall regions, where the gradient of  $\langle u_2 \rangle$  is high. Nevertheless, gradients of velocity are accurately predicted, only displaying a slight underprediction in the velocity magnitude in near-wall regions.

The turbulence shape of the developed models is represented in Fig. 12, where the reliability for both models is conserved. A certain level of anisotropy is added to the models, yielding results in the vicinity of the plain-strain limit. Both models predict a very similar turbulence shape while model II slightly yields results farther away from the plain-strain limit. Nonetheless, results are distant from  $\hat{x}_{1c}$  and DNS anisotropy. This highlights the limitations of the integration of  $T_{ij}^{(2)}$  on RANS  $k - \omega$  SST, which, while the model is robust, imposes stability limits. Although these results are expected, the integration of the whole Pope's decomposition with its 10 tensors and a more thorough definition of  $\mathcal{B}$  could be able to further improve the RANS anisotropy prediction.

### 3.3. Verification and generalisability on test cases

In this subsection, the best-found models are tested against diverse canonical cases in which secondary flow is an important component as well as cases where secondary flow is not present. This verification is performed in order to

provide a performance overview of the models' generalisability, stability, and robustness to preserve canonical flow features. Firstly, validation of the channel case and the boundary layer is performed at different Reynolds numbers. Secondly, the models are tested against diverse cases of ducts with different aspect ratios and Reynolds numbers. Lastly, the models are tested against a wall-modelled nominally-infinite Reynolds number case in which secondary flow is roughness-induced. Similarly as in section 3, all results are shown and discussed with their respective velocity contour plots with stream functions and qualitative flow analysis of the velocity profiles.

### 3.3.1. Channel flow and law of the wall

The addition of  $T_{ij}^{(2)}$  and further modification in this study must not destabilise  $k - \omega$  SST and yield unphysical results. Therefore, both models are tested in a channel flow case at friction Reynolds numbers 395 and 5200 to verify that the law of the wall is preserved. The canonical channel flow cases are driven by a constant pressure gradient in order to match the friction Reynolds number from DNS.

Results shown in Fig. 13 depict the streamwise velocity as  $u^+ = u/u_\tau$  and  $k^+ = k/u_\tau^2$  in function of  $y^+ = u_\tau y/\nu$ , where  $u_\tau$  is the friction velocity. The results show a consistent prediction of the law of the wall with  $k - \omega$  SST without introducing any notable changes. Both models yield the same results for both the streamwise velocity and the turbulence kinetic energy, and no improvements or diminishments in the prediction of these variables are seen compared to standard  $k - \omega$  SST.

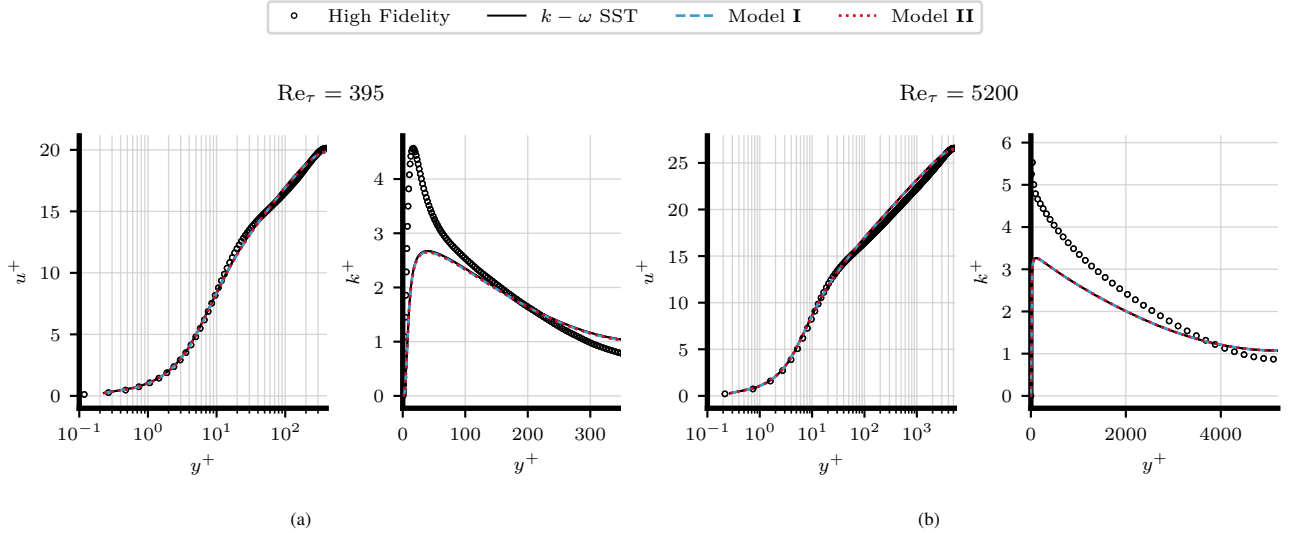


Figure 13: Mean streamwise velocity and turbulent kinetic energy profiles for channel flow:  $Re_\tau = 395$  (Fig. 13a), and  $Re_\tau = 5200$  (Fig. 13b). High-fidelity data obtained from Ref. [57].

### 3.3.2. Duct cases

To showcase the generalisability of the models, diverse duct cases are tested. The first case is the flow through a duct of  $AR = 1$  and a considerably higher  $Re_b = 5700$  compared to the optimisation case.

A qualitative depiction of the results is shown in Fig. 14, where both models are able to capture the gradients of the secondary flow and improve the prediction of the streamwise velocity compared to  $k - \omega$  SST. In agreement with the baseline results of the models, the magnitude of the secondary motion is weaker than the high-fidelity data although the motion's antisymmetry and location of the vortices centres are predicted accurately.

Regarding the velocity profiles of the case (Fig. 15), a similar trend is observed where the gradients and magnitude of the profiles are predicted with high accuracy in both models, only displaying some discrepancies in the wall-near regions, where the high-fidelity data yields slightly higher-velocity gradients.



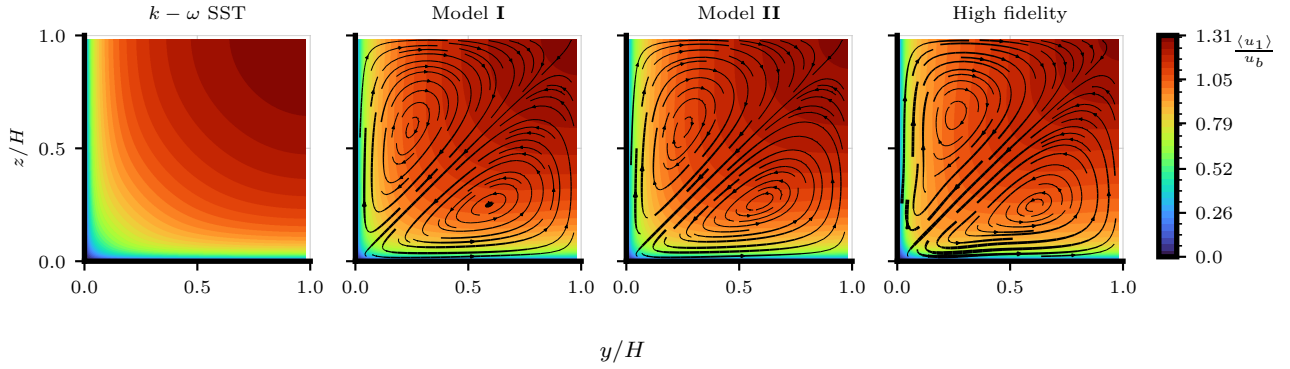


Figure 14: Streamwise flow contours with stream function iso lines depicting secondary flow prediction and direction: Duct flow case with AR = 1 and  $Re_b = 5700$ . High-fidelity data obtained from Ref. [59].

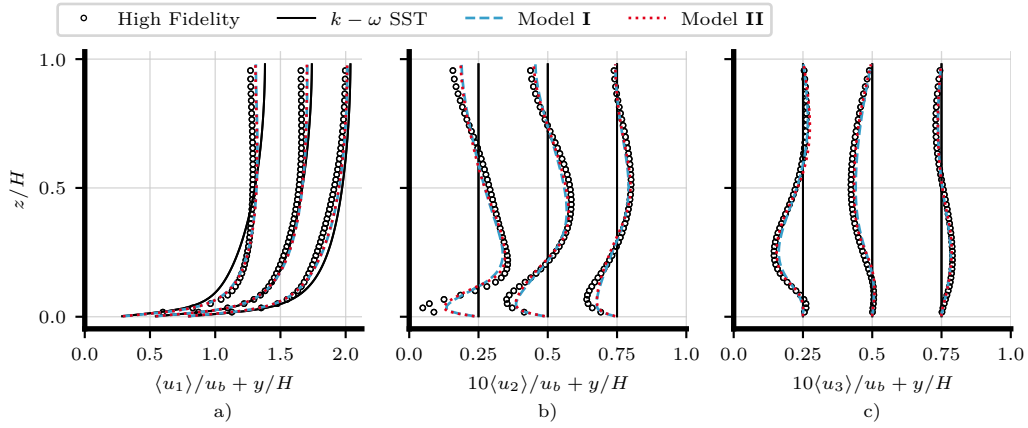


Figure 15: Profiles of velocity components for duct flow case with AR = 1 and  $Re_b = 5700$ . High-fidelity data obtained from Ref. [59].

In order to verify the performance of the models in diverse cases with similar features, the models are likewise tested against a duct of AR= 3 and a slightly lower  $Re_b = 2600$  compared to the optimisation case.

The qualitative results shown in Fig. 14 indicate a similar performance for both models: gradients, symmetry, and direction of secondary flow are predicted accurately with slight inaccuracies regarding the secondary flow magnitude in the near-wall regions. The location of the vortices centres is likewise predicted with high accuracy, agreeing with high-fidelity data (Fig. 16).

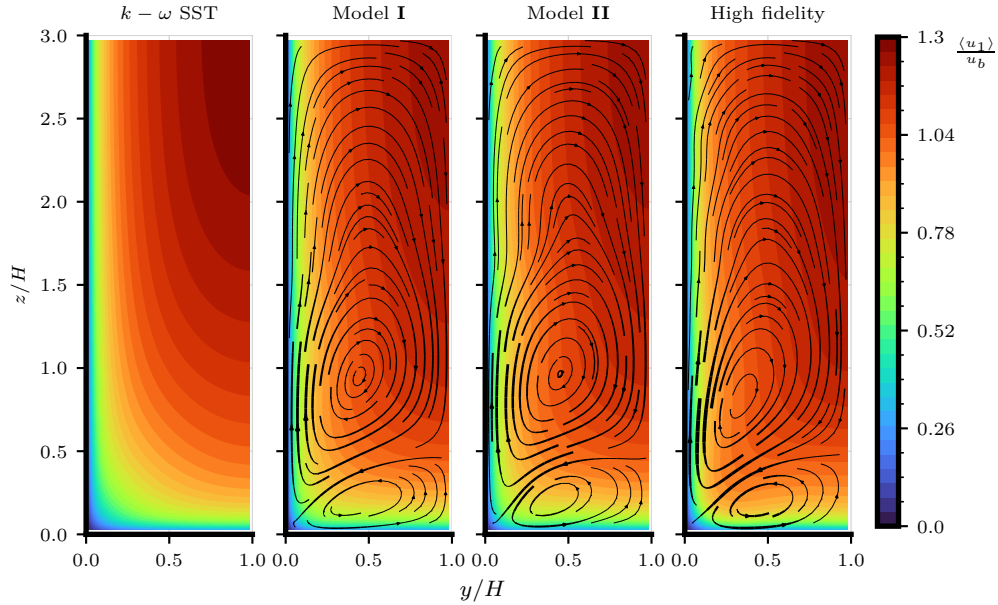


Figure 16: Streamwise flow contours with stream function iso lines depicting secondary flow prediction and direction: Duct flow case with  $AR = 3$  and  $Re_b = 2600$ . High-fidelity data obtained from Ref. [59].

In terms of the quantitative analysis and the evaluation of the velocity profiles, the results shown in Fig. 17 likewise follow a similar trend compared to previous results in this study. The region in the vicinity of the duct vertex shows some discrepancy in the velocity prediction. Nevertheless, the bulk flow away from the near wall is accurately predicted.

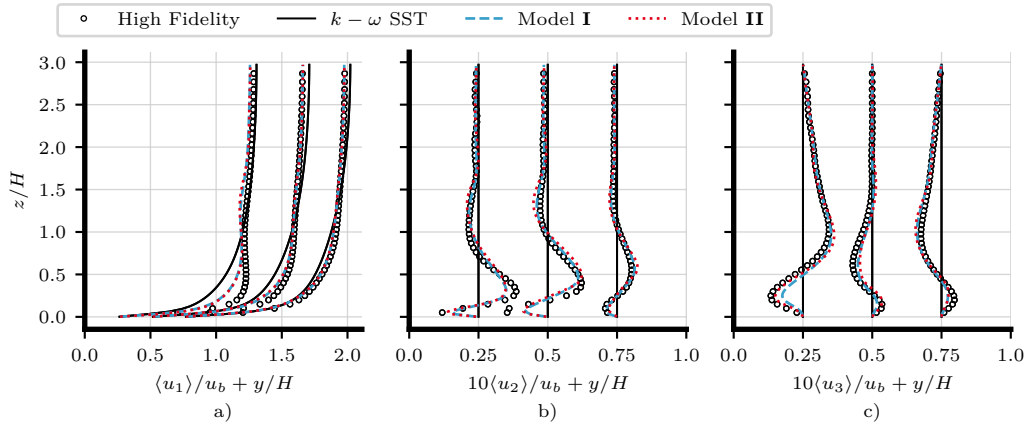


Figure 17: Profiles of velocity components for duct flow case with  $AR = 3$  and  $Re_b = 2600$ . High-fidelity data obtained from Ref. [59].

### 3.3.3. Roughness-induced secondary flow case

Finally, the verification of the models is tested on a roughness-induced secondary flow case. The case is based on the studies by [38, 39], and it is used to showcase the models' performance in a more complex case with a very high Reynolds number, and the necessary use of wall models. The secondary flows generated in this case are recognised as Prandtl's second kind of secondary flow, similar to the square duct flow [2]. Furthermore, this case is likewise known for the difficulties of two-equation RANS turbulence models to accurately predict.

For a better analysis of roughness-induced secondary flow, dispersive velocity components are defined as,

$$\langle u_i'' \rangle = \langle u_i \rangle - \langle \tilde{u}_i \rangle, \quad (22)$$

where  $\langle u_i'' \rangle$  is the dispersive velocity components, and  $\langle \tilde{u}_i \rangle$  is the spatial spanwise-averaged mean velocity.

Following previous verification, the qualitative results of the streamwise dispersive velocity ( $\langle u_1'' \rangle$ ) are shown in Fig. 18. On the one hand, results show that standard  $k - \omega$  SST does not predict any secondary motion that drives the flow to display a high-momentum path on top of the high-roughness patch and a low-momentum path at  $y/H = 0$ , as the high-fidelity data predicts. On the other hand, the enhanced models are both capable to predict the secondary motion, although at a lower intensity compared to high-fidelity results. The direction of the rotation (clockwise) is correctly predicted although the vortex centre does not visibly match the high-fidelity counterpart. Even though the predicted secondary flow is not strong enough to move the low-momentum path to the top of the low-roughness patch ( $y/H = 0$ ), the existence of a weak high-momentum path is visible on top of the high-roughness patch. Since the source of vorticity production lies at roughness-heterogeneity existing at the bottom wall (more information at Ref. [39]), the authors believe that further investigations about wall models regarding the secondary flow can help a better prediction of the secondary flow. It should be noted that because of the very high Reynolds number using the wall models is inevitable, and the atmospheric wall models [62] have been used in this case.

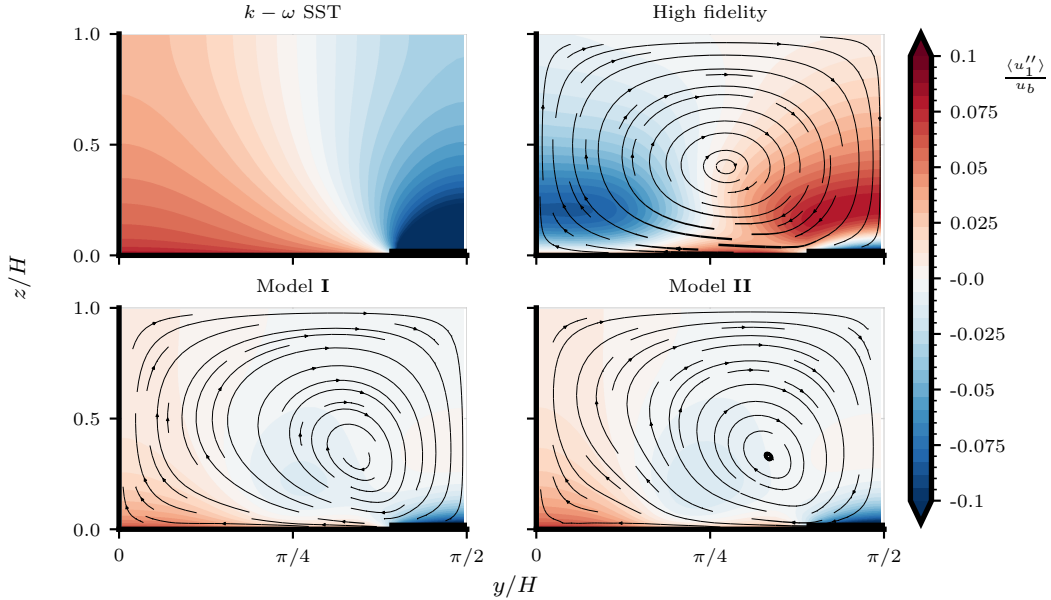


Figure 18: Streamwise dispersive velocity contours with stream function iso lines depicting secondary flow prediction and direction: Roughness-induced secondary flow case with  $Re_b = 2 \times 10^8$ . High-fidelity data obtained from Ref. [39].

Quantitative results reflect the previous qualitative analysis. Figure 19 shows the velocity profiles at  $y/H \in [\pi/8, \pi/4, 3\pi/8]$ , where the improvement of the models can be seen. In contrast to other verification cases in this study, both models' predictions improve the performance of standard  $k - \omega$  SST, however, the secondary flow intensity is weaker compared to the high-fidelity data. The predicted tendencies are correct, although there is a greater discrepancy in the gradients and magnitudes predictions relative to previous verification cases.

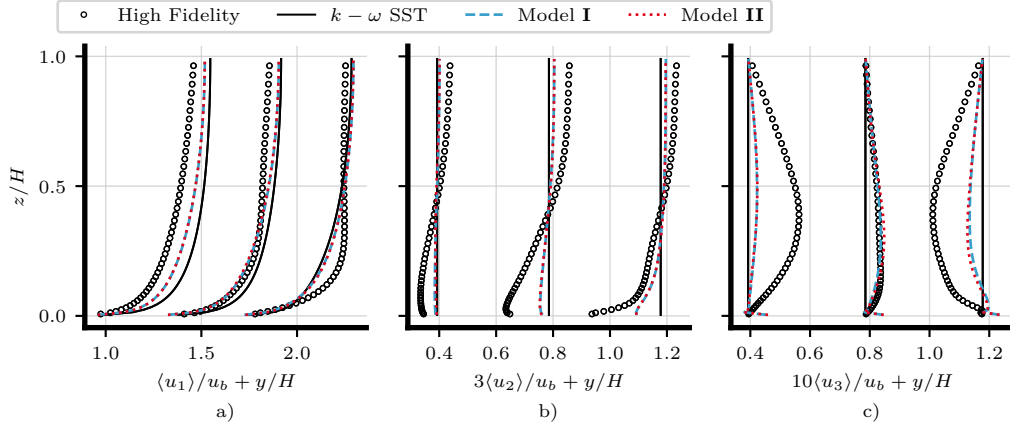


Figure 19: Profiles of velocity components for roughness-induced secondary flow with  $Re_b = 2 \times 10^8$ . High-fidelity data obtained from Ref. [39].

To provide a complete and holistic comparative study for this case, the spatial average of the streamwise, as well as vertical root-mean-squared (RMS) dispersive velocity ( $\langle \tilde{u}_1 \rangle$  and  $RMS \langle u_3'' \rangle$ , respectively), are calculated. These results are shown in Fig. 20, where the prediction of  $\langle \tilde{u}_1 \rangle$  shows a considerable improvement compared to standard  $k - \omega$  SST. However, the bulk flow for the developed models is still overpredicted as a consequence of the underpredicted secondary flow and its derived under-subtraction of the streamwise momentum. Regarding the  $RMS \langle u_3'' \rangle$ , a clear improvement in the prediction can be seen by the developed models, where  $k - \omega$  SST is unable to predict any vertical dispersive velocity. The predictive profiles are underpredicted and slightly skewed towards  $z/H = 0$  compared to the high-fidelity data, which verifies the mismatched location of the predicted secondary flow vortices. Both developed models yield an almost identical prediction of the flow, although a slight improvement is seen by model II at its prediction of  $RMS \langle u_3'' \rangle$ . Overall, the applicability of the models to this case shows their generalisability, where robust and improved predictions are obtained in more complex cases at very high Reynolds numbers.

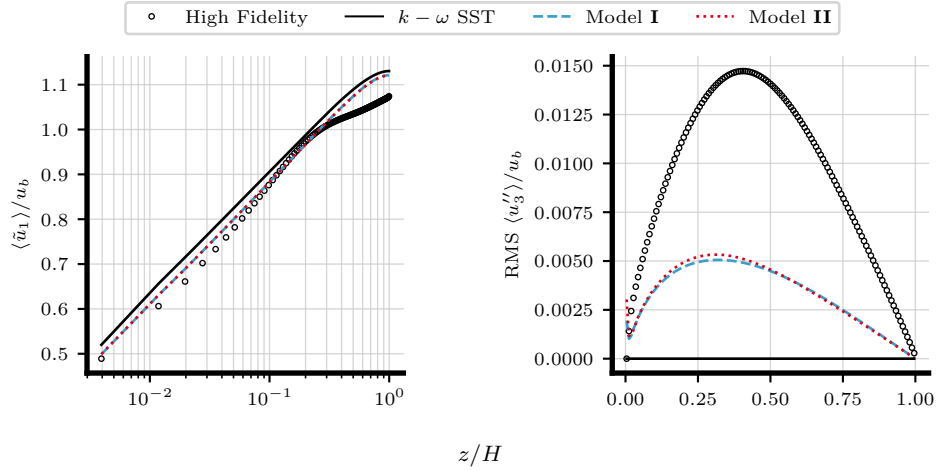


Figure 20: Roughness-induced secondary flow quantitative results of spanwise-averaged streamwise velocity (left), and root-mean-squared dispersive vertical velocity (right). High-fidelity data obtained from Ref. [39].

## 4. Conclusions

This study employs CFD-driven surrogate optimisation to enhance the  $k - \omega$  SST turbulence model focusing on predicting secondary flows. A progressive approach is adopted to enhance the linear eddy-viscosity model with the ability to predict secondary flows while maintaining its effective performance in canonical flow cases. The enhancement is based on the introduction of explicit algebraic Reynolds stress correction models with two levels of complexity: introducing a linear combination of candidate functions and introducing a linear combination of the first two principal components obtained from PCA on two candidate functions. These two models are optimised to reach the best reconstruction of both secondary flow and streamwise flow in the optimisation case of a duct flow with an aspect ratio of 1 and  $Re_b = 3500$ .

Considering the progressive approach, the enhanced models are tested against channel flow cases at different friction Reynolds numbers, where the enhanced models preserve the original performance of the  $k - \omega$  SST model in a successful reproduction of the velocity and TKE profiles compared with the high-fidelity data.

For the purpose of generalisability investigation, new models are tested against verification duct-flow cases with different Reynolds numbers and different aspect ratios. Both enhanced models show a successful reconstruction of secondary flow and improvement of streamwise velocity prediction in the unseen cases. The third and final verification case is a roughness-induced secondary flow case at a nominally-infinite Reynolds number, where the enhanced models are able to predict the secondary motion, although at a lower intensity compared to high-fidelity data due to the limitations of wall modelling for this type of cases.

Overall, the results, summarised in Table 2, show that the developed models perform substantially better than the standard  $k - \omega$  SST model in all verification cases. The enhanced models are able to capture the secondary flow features and show improvements in the velocity field prediction. However, it should be noted that the optimisation process and the nature of the EARSCMs yield a certain level of turbulence anisotropy while always maintaining solution robustness and stability. This fact results in some discrepancies between the EARSCMs and high-fidelity data in the predicted turbulence shape.

Table 2: Objective function results for optimisation case and all verification cases tested. Results are presented by the case abbreviation and characteristics: Duct flow cases as  $DF_{AR, Re}$  and roughness-induced secondary flow as  $RI_{Re}$ . It should be noted that  $DF_{1, 3500}$  is the optimisation case, and  $J = 1$  indicates the  $k - \omega$  SST original prediction and  $J = 0$  indicates a match of the high-fidelity data.

Case	Model	$J$	$j_1$	$j_2$
$DF_{1, 3500}$	<b>I</b>	0.387	0.455	0.319
	<b>II</b>	0.373	0.426	0.32
$DF_{1, 5700}$	<b>I</b>	0.405	0.482	0.328
	<b>II</b>	0.394	0.471	0.316
$DF_{3, 2600}$	<b>I</b>	0.458	0.551	0.365
	<b>II</b>	0.488	0.572	0.405
$RI_{2 \times 10^8}$	<b>I</b>	0.693	0.663	0.723
	<b>II</b>	0.697	0.662	0.732

These findings suggest that the use of CFD-driven optimisation with surrogate modelling is a robust approach to enhance linear-eddy-viscosity turbulence models to predict more complex physics. The enhanced EARSCMs developed, greatly improve the accuracy of turbulence modelling in wall-bounded flows, especially in cases where the standard  $k - \omega$  SST presents difficulties in accurately predicting the secondary flow. The progressive nature of this development as a first step focuses on the prediction of secondary flows, allowing further improvement of the models by adding more predictive physics to them and verifying them on other test cases.

### CRedit authorship contribution statement

**Mario Javier Rincón:** Conceptualisation, Methodology, Software, Validation, Formal analysis, Writing – original draft. **Ali Amarloo:** Conceptualisation, Methodology, Software, Validation, Formal analysis, Writing – original draft.

**Martino Reclari:** Formal analysis, Methodology, Writing – review & editing. **Xiang I. A. Yang:** Formal analysis, Methodology, Writing – review & editing. **Mahdi Abkar:** Conceptualisation, Methodology, Formal analysis, Project administration, Resources, Supervision, Writing – review & editing.

### Declaration of Competing Interest

The authors declare that they have no known competing financial interests or personal relationships that could have appeared to influence the work reported in this study.

### Acknowledgments

M.J.R. acknowledges the financial support from the Innovation Fund Denmark (IFD) under Grant No. 0153-00051B, and Kamstrup A/S. A.A. acknowledges the financial support from the Aarhus University Centre for Digitalisation, Big Data, and Data Analytics (DIGIT) and Aarhus University Research Foundation (AUFF).

### Data availability

The models developed in this study are publicly available for their use and compilation in OpenFOAM under <https://github.com/AUfluids/EARSCM>. Further data will be made available on request.

### References

- [1] J. Slotnick, A. Khodadoust, A. Juan, D. Darmofal, W. Groppe, E. Lurie, D. Mavriplis, CFD vision 2030 study: A path to revolutionary computational aerosciences, Technical Report NASA/CR-2014-218178, NASA (2014).
- [2] N. Nikitin, N. Popelenskaya, A. Stroh, Prandtl’s secondary flows of the second kind. Problems of description, prediction, and simulation, *Fluid Dyn.* 56 (4) (2021) 513–538.
- [3] H. Xiao, P. Cinnella, Quantification of model uncertainty in RANS simulations: A review, *Prog. Aerosp. Sci.* 108 (2019) 1–31.
- [4] K. Duraisamy, G. Iaccarino, H. Xiao, Turbulence modeling in the age of data, *Annu. Rev. Fluid Mech.* 51 (2019) 357–377.
- [5] B. Tracey, K. Duraisamy, J. Alonso, Application of supervised learning to quantify uncertainties in turbulence and combustion modeling, in: 51st AIAA aerospace sciences meeting including the new horizons forum and aerospace exposition, 2013, p. 259.
- [6] J.-X. Wang, J.-L. Wu, H. Xiao, Physics-informed machine learning approach for reconstructing Reynolds stress modeling discrepancies based on DNS data, *Phys. Rev. Fluids* 2 (3) (2017) 034603.
- [7] J.-L. Wu, H. Xiao, E. Paterson, Physics-informed machine learning approach for augmenting turbulence models: A comprehensive framework, *Phys. Rev. Fluids* 3 (7) (2018) 074602.
- [8] J. Ling, A. Kurzawski, J. Templeton, Reynolds averaged turbulence modelling using deep neural networks with embedded invariance, *J. Fluid Mech.* 807 (2016) 155–166.
- [9] M. L. Kaandorp, R. P. Dwight, Data-driven modelling of the Reynolds stress tensor using random forests with invariance, *Comput. Fluids* 202 (2020) 104497.
- [10] R. McConkey, E. Yee, F.-S. Lien, Deep structured neural networks for turbulence closure modeling, *Phys. Fluids* 34 (3) (2022) 035110.
- [11] M. A. Cruz, R. L. Thompson, L. E. Sampaio, R. D. Bacchi, The use of the Reynolds force vector in a physics informed machine learning approach for predictive turbulence modeling, *Comput. Fluids* 192 (2019) 104258.
- [12] J. Weatheritt, R. Sandberg, A novel evolutionary algorithm applied to algebraic modifications of the RANS stress–strain relationship, *J. Comput. Phys.* 325 (2016) 22–37.
- [13] J. Weatheritt, R. Sandberg, The development of algebraic stress models using a novel evolutionary algorithm, *Int. J. Heat Fluid Flow* 68 (2017) 298–318.
- [14] M. Schmelzer, R. P. Dwight, P. Cinnella, Discovery of algebraic Reynolds-stress models using sparse symbolic regression, *Flow Turbul. Combust.* 104 (2) (2020) 579–603.
- [15] A. Amarloo, P. Forooghi, M. Abkar, Frozen propagation of Reynolds force vector from high-fidelity data into Reynolds-averaged simulations of secondary flows, *Phys. Fluids* 34 (11) (2022) 115102.
- [16] K. Duraisamy, Perspectives on machine learning-augmented Reynolds-averaged and large eddy simulation models of turbulence, *Phys. Rev. Fluids* 6 (5) (2021) 050504.
- [17] A. P. Singh, S. Medida, K. Duraisamy, Machine-learning-augmented predictive modeling of turbulent separated flows over airfoils, *AIAA J.* 55 (7) (2017) 2215–2227.
- [18] J. R. Holland, J. D. Baeder, K. Duraisamy, Field inversion and machine learning with embedded neural networks: Physics-consistent neural network training, in: *AIAA Aviation 2019 Forum*, 2019, p. 3200.
- [19] Y. Zhao, H. D. Akolekar, J. Weatheritt, V. Michelassi, R. D. Sandberg, RANS turbulence model development using CFD-driven machine learning, *J. Comput. Phys.* 411 (2020) 109413.
- [20] I. B. H. Saïdi, M. Schmelzer, P. Cinnella, F. Grasso, CFD-driven symbolic identification of algebraic Reynolds-stress models, *J. Comput. Phys.* 457 (2022) 111037.

- [21] J. Barzilai, J. M. Borwein, Two-point step size gradient methods, *IMA J. Numer. Anal.* 8 (1) (1988) 141–148.
- [22] J. A. Nelder, R. Mead, A Simplex Method for Function Minimization, *Comput. J.* 7 (4) (1965) 308–313.
- [23] C. A. C. Coello, G. B. Lamont, D. A. Van Veldhuizen, et al., *Evolutionary algorithms for solving multi-objective problems*, Vol. 5, Springer, (2007).
- [24] R. Eberhart, J. Kennedy, Particle swarm optimization, in: *Proceedings of the IEEE international conference on neural networks*, Vol. 4, Citeseer, 1995, pp. 1942–1948.
- [25] M. J. Rincón, M. Reclari, M. Abkar, Turbulent flow in small-diameter ultrasonic flow meters: A numerical and experimental study, *Flow Meas. Instrum.* 87 (2022) 102227.
- [26] M. J. Rincón, M. Reclari, X. I. Yang, M. Abkar, Validating the design optimisation of ultrasonic flow meters using computational fluid dynamics and surrogate modelling, *Int. J. Heat Fluid Flow* 100 (2023) 109112.
- [27] P. Singh, I. Couckuyt, K. Elsayed, D. Deschrijver, T. Dhaene, Multi-objective geometry optimization of a gas cyclone using triple-fidelity co-kriging surrogate models, *J. Optim. Theory Appl.* 175 (1) (2017) 172–193.
- [28] X. Lam, Y. Kim, A. Hoang, C. Park, Coupled aerostructural design optimization using the kriging model and integrated multiobjective optimization algorithm, *J. Optim. Theory Appl.* 142 (3) (2009) 533–556.
- [29] M. Urquhart, M. Varney, S. Sebben, M. Passmore, Aerodynamic drag improvements on a square-back vehicle at yaw using a tapered cavity and asymmetric flaps, *Int. J. Heat Fluid Flow* 86 (2020) 108737.
- [30] F. Waschkowski, Y. Zhao, R. Sandberg, J. Klewicki, Multi-objective CFD-driven development of coupled turbulence closure models, *J. Comput. Phys.* 452 (2022) 110922.
- [31] X. L. Huang, X. I. Yang, A bayesian approach to the mean flow in a channel with small but arbitrarily directional system rotation, *Phys. Fluids* 33 (1) (2021) 015103.
- [32] T.-R. Xiang, X. Yang, Y.-P. Shi, Neuroevolution-enabled adaptation of the jacobi method for poisson’s equation with density discontinuities, *Theor. App. Mech. Lett.* 11 (3) (2021) 100252.
- [33] R. D. Sandberg, Y. Zhao, Machine-learning for turbulence and heat-flux model development: A review of challenges associated with distinct physical phenomena and progress to date, *Int. J. Heat Fluid Flow* 95 (2022) 108983.
- [34] Y. Fang, Y. Zhao, F. Waschkowski, A. S. Ooi, R. D. Sandberg, Toward more general turbulence models via multicase computational-fluid-dynamics-driven training, *AIAA J.* (2023) 1–16.
- [35] Y. Bin, L. Chen, G. Huang, X. I. Yang, Progressive, extrapolative machine learning for near-wall turbulence modeling, *Phys. Rev. Fluids* 7 (8) (2022) 084610.
- [36] F. R. Menter, Two-equation eddy-viscosity turbulence models for engineering applications, *AIAA J.* 32 (8) (1994) 1598–1605.
- [37] S. B. Pope, A more general effective-viscosity hypothesis, *J. Fluid Mech.* 72 (2) (1975) 331–340.
- [38] P. Forooghi, X. I. Yang, M. Abkar, Roughness-induced secondary flows in stably stratified turbulent boundary layers, *Phys. Fluids* 32 (10) (2020) 105118.
- [39] A. Amarloo, P. Forooghi, M. Abkar, Secondary flows in statistically unstable turbulent boundary layers with spanwise heterogeneous roughness, *Theor. App. Mech. Lett.* 12 (2) (2022) 100317.
- [40] S. B. Pope, *Turbulent flows*, Cambridge University Press, (2000).
- [41] F. R. Menter, M. Kuntz, R. Langtry, Ten years of industrial experience with the sst turbulence model, *Turbul. Heat Mass Transf.* 4 (1) (2003) 625–632.
- [42] J. Sacks, S. B. Schiller, W. J. Welch, Designs for Computer Experiments, *Technometrics* 31 (1) (1989) 41–47.
- [43] H. G. Weller, G. Tabor, H. Jasak, C. Fureby, A tensorial approach to computational continuum mechanics using object-oriented techniques, *Comput. phys.* 12 (6) (1998) 620–631.
- [44] M. D. McKay, R. J. Beckman, W. J. Conover, A comparison of three methods for selecting values of input variables in the analysis of output from a computer code, *Technometrics* 42 (1) (2000) 55–61.
- [45] R. Jin, W. Chen, A. Sudjianto, An efficient algorithm for constructing optimal design of computer experiments, *J. Stat. Plan.* 134 (1) (2005) 268–287.
- [46] G. Damblin, M. Couplet, B. Iooss, Numerical studies of space-filling designs: optimization of Latin Hypercube Samples and subprojection properties, *J. Simul.* 7 (4) (2013) 276–289.
- [47] S. Kawai, K. Shimoyama, Kriging-model-based uncertainty quantification in computational fluid dynamics, in: *32nd AIAA Applied Aerodynamics Conference*, 2014, p. 2737.
- [48] M. A. Bouhlel, J. T. Hwang, N. Bartoli, R. Lafage, J. Morlier, J. R. R. A. Martins, A Python surrogate modeling framework with derivatives, *Adv. Eng. Softw.* (2019) 102662.
- [49] A. Sobester, A. Forrester, A. Keane, *Engineering design via surrogate modelling: a practical guide*, John Wiley & Sons, (2008).
- [50] T. Hastie, R. Tibshirani, J. H. Friedman, J. H. Friedman, *The elements of statistical learning: data mining, inference, and prediction*, Vol. 2, Springer, (2009).
- [51] D. R. Jones, A taxonomy of global optimization methods based on response surfaces, *J. Glob. Optim.* 21 (4) (2001) 345–383.
- [52] D. R. Jones, M. Schonlau, W. J. Welch, Efficient global optimization of expensive black-box functions, *J. Glob. Optimiz.* 13 (4) (1998) 455–492.
- [53] J. Mockus, V. Tiesis, A. Zilinskas, The application of Bayesian methods for seeking the extremum, *Toward. Glob. Optimiz.* 2 (117–129) (1978) 2.
- [54] K. Deb, A. Pratap, S. Agarwal, T. Meyarivan, A fast and elitist multiobjective genetic algorithm: NSGA-II, *IEEE Trans. Evol. Comput.* 6 (2) (2002) 182–197.
- [55] A. Pinelli, M. Uhlmann, A. Sekimoto, G. Kawahara, Reynolds number dependence of mean flow structure in square duct turbulence, *J. Fluid Mech.* 644 (2010) 107–122.
- [56] R. McConkey, E. Yee, F.-S. Lien, A curated dataset for data-driven turbulence modelling, *Sci. Data* 8 (1) (2021) 1–14.
- [57] R. D. Moser, J. Kim, N. N. Mansour, Direct numerical simulation of turbulent channel flow up to  $re_{\tau} = 590$ , *Phys. Fluids* 11 (4) (1999) 943–945.

- [58] M. Lee, R. D. Moser, Direct numerical simulation of turbulent channel flow up to, *J. Fluid Mech.* 774 (2015) 395–415.
- [59] R. Vinuesa, P. Schlatter, H. Nagib, Secondary flow in turbulent ducts with increasing aspect ratio, *Phys. Rev. Fluids* 3 (5) (2018) 054606.
- [60] S. D. Hornshøj-Møller, P. D. Nielsen, P. Foroughi, M. Abkar, Quantifying structural uncertainties in Reynolds-averaged Navier–Stokes simulations of wind turbine wakes, *Renew. Energy* 164 (2021) 1550–1558.
- [61] M. Emory, G. Iaccarino, Visualizing turbulence anisotropy in the spatial domain with componentality contours, *Center for Turbulence Research Annual Research Briefs* (2014) 123–138.
- [62] A. Parente, C. Gorié, J. Van Beeck, C. Benocci, Improved  $k$ – $\varepsilon$  model and wall function formulation for the RANS simulation of abl flows, *J. Wind Eng. Ind. Aero* 99 (4) (2011) 267–278.